Real-Time Diagnosis of Open Circuit Faults in Three-Phase Voltage Source Inverters

Yu Luo, Li Zhang, *Senior Member, IEEE*, Chunyang Chen, Kang Li, *Senior Member, IEEE*, and Kaidi Li

***Abstract*—This article investigates the real-time diagnosis of single and double open circuit faults (OCFs) in three-phase voltage source inverters (VSIs). The method analyzes the phase current waveforms continuously in real-time, and abnormal patterns of the current waves due to the corresponding switch OCFs are extracted to define as the fault detection waveforms (FDW). The current values of the FDWs are analyzed and a new scheme is developed to distinguish current waveform patterns from those of normal to unbalanced loads situations and switch OCFs. The scheme detects the starting zero crossing point first and then checks the magnitudes of the FDW. Periodic detections are applied to identify whether the collected data samples are within the FDW current range. The OCFs of the inverter switches are identified by counting the fault points within the predicted samplings of FDWs. The method has been verified through both simulations and experiments. The results confirm the effectiveness of the proposed scheme.**

***Index Terms*—Current samples, fault diagnosis, open circuit fault (OCF), unbalanced load, voltage source inverter (VSI).**

I. Introduction

THREE-PHASE voltage source inverters (VSIs) are capable of converting electrical energy from dc power sources, including batteries, solar cells, or fuel cells, into ac voltages with flexible frequencies and amplitudes. Due to their high efficiency and control flexibility, three-phase VSIs play a vital role in modern industrial and energy sectors [1], [2]. The power semiconductor switch devices commonly employed in three-phase VSIs are metal-oxide-semiconductor field-effect transistors (MOSFETS) and insulated-gate bipolar transistors (IGBTs) [3], [4]. Recent advancements in power device manufacturing have led to the widespread utilization of wide bandgap materials, such as silicon carbide (SiC) or gallium nitride (GaN) in inverters [5], [6]. Switch failures are a prevalent issue in three-phase inverters, which rely on power semiconductor switch devices that are relatively delicate and subject to high voltage stress [7], [8].

Such switches in inverters are susceptible to short-circuit and open-circuit faults (OCFs). Short-circuit faults are highly destructive, causing high current flow, but are typically detected by standard protection systems such as fuses and circuit breakers, resulting in an immediate shutdown of the inverter [9], [10]. In contrast, implementing OCF protection requires additional circuits and equipment, with an increase in manufacturing cost and complexity of the inverter. Consequently, OCF protection is not typically included as a standard offer in industrial applications [11], [12]. However, OCFs can also lead to drive circuit and load failures, and other secondary faults. Fast and accurate methods for diagnosing OCFs are therefore crucial to prevent faults from propagating to other parts of the system [13], [14]. OCF diagnosis is also essential for preventing prolonged operation with faulty switches, which can result in distorted output waveforms, abnormal load operation, and overheating [15].

In the voltage-based methods, the actual voltage can be obtained from additions to the functional circuitry or from dedicated voltage sensors. Simple hardware circuits as described in [16] and [17] can achieve diagnosis in a very short period of time. On the other hand, to reduce the need for extra hardware, a mixed logical-dynamical or switch function model can be established [18], [19], [20], [21]. In [18], a voltage envelope line is generated by the proposed voltage envelope function. By comparing the preprocessed diagnostic eigenvalue and the voltage envelope, OCFs can be located precisely. This is a highly reliable method but is limited to diagnosing a single switch OCF. As shown in [19], faults can be quickly diagnosed from the ratio, the difference, and the arithmetic values, of the two line voltages. The results show that the proposed method is robust to load variation and immune to certain load OCFs, but the robustness and reliability need to be improved when the load is a motor or motors. In [20], faults are defined by analyzing the voltage patterns in the Alpha–Beta plane. The proposed method can identify all possible types of switch OCFs in a three-phase inverter and locate the faulty switches without complex calculations or additional hardware. The drawback of this method is its limited adaptability to various loads, exhibiting poor robustness. In [21], the voltage between the midpoints of the dc side and ac side is utilized for detecting OCFs and determining the upper and lower positions of the faulty switch. The diagnostic process is fast but again is limited to diagnosing single-switch OCFs.

Manuscript received 28 August 2023; revised 13 November 2023 and 14 January 2024; accepted 18 February 2024. Date of publication 29 February 2024; date of current version 19 April 2024. This work was supported by the Fundamental Research Funds for Central Universities of the Central South University under Grant 2018zzts164. Recommended for publication by Associate Editor D. O Neacsu. *(Corresponding author: Kaidi Li.)*

Yu Luo and Chunyang Chen are with the School of Traffic and Transportation Engineering, Central South University, Changsha 410075, China (e-mail: 174201007@csu.edu.cn; cychen999@csu.edu.cn).

Li Zhang and Kang Li are with the School of Electrical Engineering, University of Leeds, LS2 9JT Leeds, U.K. (e-mail: l.zhang@leeds.ac.uk; k.li1@leeds.ac.uk).

Kaidi Li is with the Shenzhen Metro Group, Shenzhen 518000, China (e-mail: likaidi@shenzhenmc.com).

Color versions of one or more figures in this article are available at https://doi.org/10.1109/TPEL.2024.3371452.

Digital Object Identifier 10.1109/TPEL.2024.3371452

The OCF diagnosis method based on current features exhibits high sensitivity, real-time capability, reliability, and a certain level of robustness, enabling effective detection and location of OCFs in three-phase inverters. In [22], the zero voltage vector sampling method is used to sample current during the two zero voltage vectors and reconstruct the three-phase currents. These are used to generate the diagnostic variables that can detect and locate faulty power switches. The method has a good and fast diagnostic response to OCFs, but it is very poor at handling load variations. It relies heavily on the accuracy of the basic model parameters. In [23], the sum of the absolute values of the normalized phase currents is calculated, and the current zero-crossing detection method is used to avoid the influence of current distortion caused by the transient condition; the fault detection signal is built to precisely localize the faulty switches. The method has limited capability in detecting all the fault types and also lacks robustness to load variations. In [24], the OCFs of the inverter lead to output phase current distortion. Different types of faults have different space trajectories, and the corresponding fault feature is located by the direction vector and center-of-mass coordinate. The faults are diagnosed by the fault feature. This method is effective in handling certain load variation scenarios and is capable of handling multiple fault conditions. However, it does not take into account OCFs in cases of load unbalance. In [25], the three-phase current signal is decomposed into the trend, seasonal, and remainder components through the simplified seasonal trend decomposition algorithm. The thresholds of characteristic quantities are set, and a diagnosis algorithm is designed to detect the OCFs. The complexity of the algorithms involved demands an appreciable amount of diagnostic time. In [26], a unique faulty characteristics of diagnosis variables for each fault are extracted by combining two kinds of diagnosis variables, line voltage deviations and phase voltage deviations to distinguish the fault. This method exhibits a very fast response speed in fault diagnosis; however, it can only handle single OCFs. In addition, it has the drawbacks of poor capability to handle load variations with low reliability.

Over the past few years, there has been a considerable amount of research using model-based fault diagnosis for inverter drive systems. In [27], a method based on calculated average bridge arm pole-to-pole voltages and error-adaptive thresholds is presented for diagnosing the OCFs. This method demonstrates good diagnostic capabilities for various faults; however, it has certain computational requirements and relies on signals from a closed-loop controller for detection. In [28], a new fault feature extraction method is proposed to analyze the asymmetrical output signals. It is not affected by asymmetric interference. The fault diagnosis time of this method is short; however, it is limited in terms of the number of fault types it can handle, and it requires high computational capability. In [29], based on the vector decomposition principle and volt–second balancing theory, the output phase voltage model is established considering neutral point voltage unbalance and time-offset injection. The faults can be located by building two suspected phase voltage models to approximate the real system. The fault diagnosis algorithm of this method is complex, and there is room for improvement in its capability to handle load variations.

Intelligent technologies have become a hot research topic in fault diagnosis for three-phase inverters, as they possess characteristics, such as automation, data-driven analysis, the ability to diagnose multiple fault types, self-learning and adaptability, as well as remote monitoring and management. In [30], transient time-domain sequence data under different faults are analyzed, and raw signals are taken as fault representations with an automatic learn and extract method. An end-to-end method based on an improved convolutional neural network model has been proposed for inverter fault diagnosis. The computational requirements of this method are moderate; however, It can only handle single OCFs and diagnosis accuracy is affected by load variations. In [31], an extreme learning machine model is trained by the data from the source system to form an initial diagnostic model. After that, a model adaption process is designed to adjust the model parameters by minimizing the distribution divergence between the data from the source and target systems. This method is capable of handling scenarios with varying load conditions and exhibits strong transfer learning capabilities, albeit requiring a certain level of computational resources. In [32], parallel structural stacked long short-term memory (LSTM) networks are constructed, the attention mechanism is applied to weight these features adaptively and the fault is identified by features that integrate multiple sources of information. If supported by high computational power, this method can effectively diagnose faults. However, it does not take into account scenarios with load variations.

Motivated by the aforementioned techniques, this paper presents a real-time, cost-effective method for OCF diagnosis in three-phase VSIs. The method identifies the feature changes of the current waveforms, which are defined as the fault detection waveforms (FDWs), when switch OCF occurs. It can locate the faulty switches through statistical analysis of current half-waves in each phase of the VSI. The scheme analyses the distinctive fault characteristics of FDW to identify the conditions from normal to unbalanced load and switch OCFs. The procedure developed employs statistical analysis to detect the faults of the inverter switches by counting fault points within the FDWs. The proposed method offers notable advantages over existing approaches, including fast fault detection, precise fault localization, low calculation burden, and high robustness. It enables real-time diagnosis without necessitating additional hardware, leveraging the existing equipment employed for regular operation. The method has the potential to find wide-ranging applications in traction drive systems, as well as general mechanical drive systems.

The rest of this article is organized as follows. Section II introduces the inverter topology and basic mathematical modeling of the VSI, and different fault scenarios. Section III analyzes the FDWs for each switch, the variations of fault current values during OCFs in the inverter, and the impact of unbalanced loads. In Section IV, the diagnosis method based on FDWs of current values is elaborated, including fault detection and clear misdiagnoses. In Section V, the proposed fault diagnosis method is validated through MATLAB Simulink simulations based on a model of a train air conditioning inverter. The experimental platform used to validate the proposed diagnostic method is

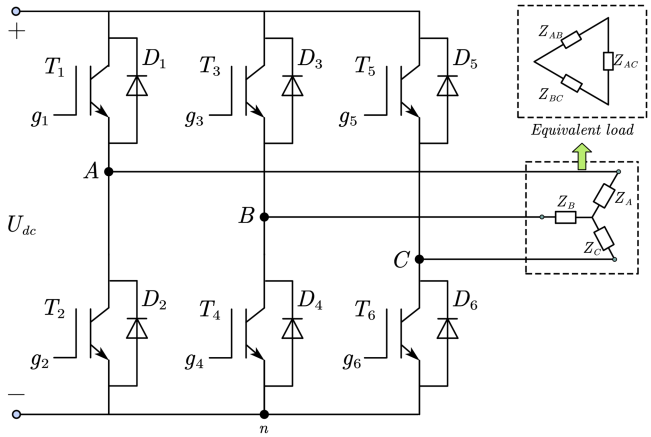

Fig. 1. Topology of three phase inverter.

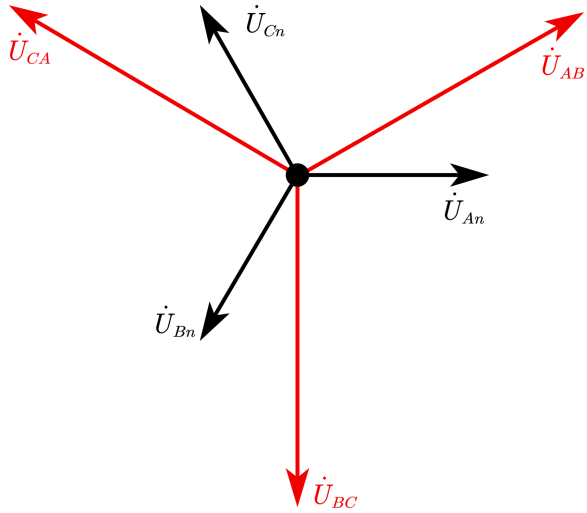

Fig. 2. Voltage vectors generated by a three-phase inverter.

introduced in Section VI, and the experimental results confirm the effectiveness and feasibility of the proposed method in comparison with different diagnosis methods. Finally, Section VII concludes this article.

II. VSI Current and Fault Classification

A. Three-Phase VSI Load Impedance and Transformation

Fig. 1 depicts a typical three-phase two-level VSI consisting of three-phase legs with six semiconductor switches (T_1–T_6) and their corresponding six freewheeling diodes (D_1–D_6). In engineering applications, a load connected to the inverter such as an induction motor is usually star-connected with its three stator windings having the same number of distributed coils with identical number of turns. Thus, the load phase impedance values are equal and well-balanced i.e., $Z_a = Z_b = Z_c = Z_Y$. As illustrated in Fig. 1, a star-connected load can be transformed to its equivalent delta-connected form. The phase impedance, in this case, can be expressed by the following equations:

$$\begin{cases} Z_{AB} = Z_A + Z_B + \frac{Z_A Z_B}{Z_C} \\ Z_{BC} = Z_B + Z_C + \frac{Z_B Z_C}{Z_A} \\ Z_{AC} = Z_A + Z_C + \frac{Z_A Z_C}{Z_B} \end{cases}. \tag{1}$$

With the three-phase load having the same impedance, the corresponding equivalent impedances from (1) are equal, $Z_{AB} = Z_{BC} = Z_{AC} = Z_\Delta$. The VSI supplies a three-phase switch mode voltage, which synthesizes three-phase sinusoidal voltage to the load with equal amplitude and phase angle difference of 120° between each phase, the phasor expressions of the voltages are given as

$$\begin{cases} \dot{U}_{An} = U_m e^{j\omega t} \\ \dot{U}_{Bn} = U_m e^{j\omega t - 2\pi/3} \\ \dot{U}_{Cn} = U_m e^{j\omega t - 4\pi/3} \end{cases} \tag{2}$$

where U_m is the magnitude of the phase voltage. Fig. 2 illustrates the vector relationship between the phase and line-line voltages.

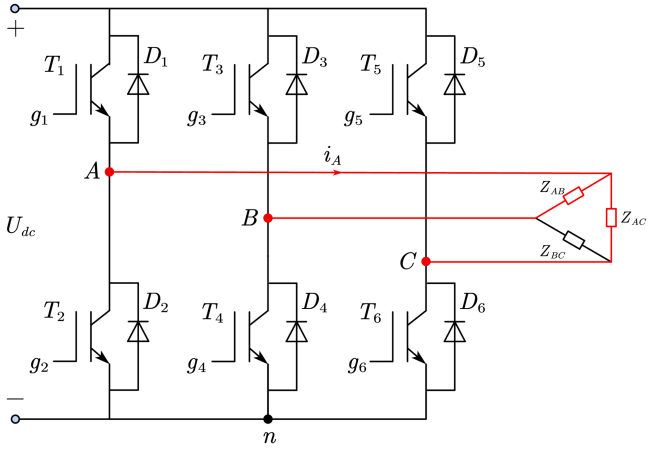

Fig. 3. Path of phase A current flow in three-phase VSI.

The line voltages of the three-phase inverter can be written as

$$\begin{cases} \dot{U}_{AB} = \sqrt{3} U_m e^{j\omega t + \pi/6} \\ \dot{U}_{BC} = \sqrt{3} U_m e^{j\omega t - \pi/2} \\ \dot{U}_{CA} = \sqrt{3} U_m e^{j\omega t + 5\pi/6} \end{cases}. \tag{3}$$

Consider six switches in a VSI shown in Fig. 3, when T_1, T_4, and T_6 are turned ON, according to Kirchhoff's current law, the current flowing through phase A is the sum of the current generated by the line voltage U_{AB} applied to the load Z_{AB} and that generated by the line voltage U_{AC} applied to the load Z_{AC}. Fig. 3 illustrates the path of the current flow of phase A under this condition. Therefore, the equation for calculating the current of phase A is given by

$$\dot{I}_A = \frac{\dot{U}_{AB}}{Z_{AB}} + \frac{\dot{U}_{AC}}{Z_{AC}}. \tag{4}$$

B. Fault Cases for a Three-Phase VSI

In practice, single-switch or double-switch OCFs are the most common in three-phase VSIs [31], Table I lists 22 types of

TABLE I
FAULT CLASSIFICATION AND LABELS

Case	Faulty switch	Case	Faulty switch
Normal	No fault	III	T_1, T_6
I	T_1		T_2, T_3
	T_2		T_3, T_6
	T_3		T_2, T_5
	T_4		T_4, T_5A
	T_5	IV	T_1, T_3
	T_6		T_1, T_5
II	T_1, T_2		T_3, T_5
	T_3, T_4		T_2, T_4
	T_5, T_6		T_2, T_6
III	T_1, T_4		T_4, T_6

inverter operating conditions, including one normal operation and 21 OCF conditions. The fault conditions are divided into four categories.

Case I: Single OCF.

Case II: Two OCFs in the same phase inverter leg.

Case III: Two OCFs occurring on two different phase inverter legs and on different sides of a three-phase VSI.

Case IV: Two OCFs on two different phase inverter legs at the same top or bottom side of a three-phase VSI.

III. FAULT CURRENT ANALYSIS

1) FDW for Each Switch: The operation of each inverter phase can be divided into two states, the inserted state and the bypassed state, based on the gate signals applied to the corresponding switches. Taking phase A as an example, when $T_1 = 1$ and $T_2 = 0$, phase A is in the inserted state (1 indicates the switch is ON, while 0 indicates the switch is OFF). Similarly, when $T_1 = 0$ and $T_2 = 1$, phase A is in the bypassed state. To describe these two states clearly, the switching function S_A can be defined as

$$S_A = \begin{cases} 1 & T_1 = 1 \ \& \ T_2 = 0 \ \text{(inserted)} \\ 0 & T_1 = 0 \ \& \ T_2 = 1 \ \text{(bypassed)} \end{cases}. \tag{5}$$

This is also applied to phases B and C.

When an OCF occurs in a three-phase VSI, it results in a change in the current flowing through the faulty switch. Fig. 4 illustrates the effect of a fault occurring in switch T_1 on the phase A current. Fig. 4(a) shows the operation mode when $i_A > 0$, $S_A = 1$ and T_1 has OCF.

Under normal condition, there may be a current flowing from the positive dc terminal, like i_{dc} through switch T_1 to ac terminal A. However, since T_1 has OCF, i_{dc} will not pass through T_1 to phase A. The current i_A is drastically reduced and not equal to i_{dc}.

Fig. 4(b) shows the situation when $i_A > 0$, $S_A = 0$ and T_1 OCF. Under the normal condition, $S_A = 0$ means T_1 is bypassed but there is still a current path through T_2 or its freewheeling diode D_2. The current is either a reactive current or from the other parts of the circuit such as phases B and C. So, when T_1 has OCF, i_A is not affected, since the current flowing path is the freewheeling diode D_2.

Fig. 4(c) shows another situation when $i_A < 0$, $S_A = 1$ and T_1 has OCF. In this case, under the normal condition, i_A is

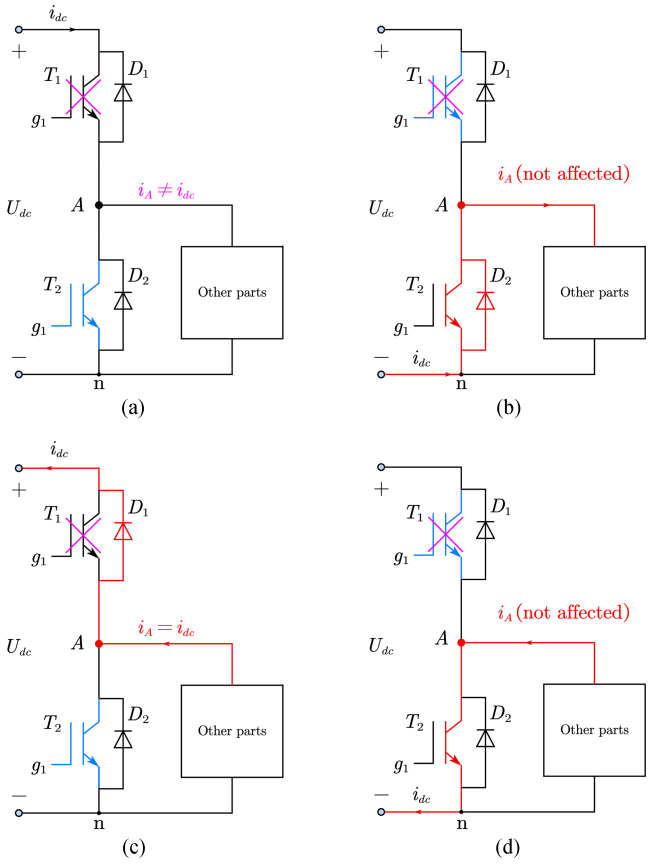

Fig. 4. Current analysis of T_1 fault. (a) $S_A = 1$, T_1 fault & $i_A > 0$. (b) $S_A = 0$, T_1 fault & $i_A > 0$. (c) $S_A = 1$, T_1 fault & $i_A < 0$. (d) $S_A = 0$, T_1 fault & $i_A < 0$.

TABLE II
FDW OF SIX SWITCHES

Switch	Phase	Halfwave	Switch	Phase	Halfwave
T_1	A	+	T_2	A	−
T_3	B	+	T_4	B	−
T_5	C	+	T_6	C	−

negative flowing from A to the positive terminal of the dc source through its freewheeling diode D_1. Thus, the flow path of i_A is unaffected.

Fig. 4(d) depicts another scenario, switch T_1 is bypassed even though it has OCF, there is no effect on the magnitude of current i_A.

To summarize from the above, when an OCF occurs on switch T_1, i_A will be drastically reduced only in the situation shown in Fig. 4(a), when its current is positive. Therefore, to detect OCF on T_1, we need to monitor the behavior of the phase A current during the positive half-cycle, which is defined as the FDW for T_1.

The same analysis as above can be applied to the other switches for detecting their OCF conditions. Table II describes FDWs for the six switches. For switches T_3 and T_5, their FDW are the positive half-cycle wave of phases B and C, respectively. The FDWs of switches T_2, T_4, and T_6 are the negative half-cycle period of phases A, B, and C currents, respectively.

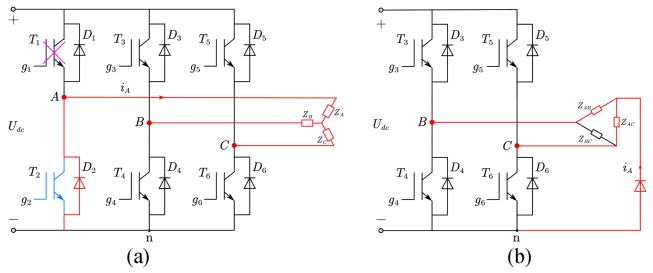

Fig. 5. Phase A current circuit when T_1 OCF ($S_A = 0, i_A > 0$).

2) Current Analysis Under Different Fault Cases: Taking switch T_1 as an example, based on the fault classification listed in Table I, the possible operation scenarios for a VSI include the following three types:

a) The inverter is in normal operation condition.
b) Six separate cases all involving T_1 having OCF (see Table I), these are

Case I: T_1 OCF.
Case II: T_1 and T_2 OCF.
Case III: T_1 and T_4, or T_1 and T_6 OCF.
Case IV: T_1 and T_3 or T_1 and T_5 OCF.

c) T_1 is not faulty but the other five switches have OCF separately.

For scenarios (a) above, phase A current is a normal sinusoidal. However for scenarios (b), Case I, phase A current i_A is significantly reduced compared to that under normal condition with the same load as shown in Fig. 4(a) and (b).

Fig. 5 shows the current i_A flowing path when T_1 has OCF. The current originates from the other part of the inverter and passes the ON-state switch T_2 or the freewheeling diode D_2.

Assuming the three-phase load is a star (Y) connected as shown in Fig. 5(a), it can be transformed to the equivalent delta (Δ) load for analysis as shown in Fig. 5(b), using (1). This is primarily to simplify the analysis for a better understanding of the relationships between the OCF current and normal current.

Fig. 5(b) shows the equivalent circuit of Fig. 5(a). According to Kirchhoff's current law, the output current of phase A, shown in Fig. 5(b), is the sum of the current generated by V_{Bn} applied on the Z_{AB} load and that generated by V_{Cn} applied on the Z_{AC} load, namely

$$\dot{I}_{\text{A\_fault}} = \frac{\dot{U}_{Bn}}{Z_{AB}} + \frac{\dot{U}_{Cn}}{Z_{AC}} \tag{6}$$

When the load is balanced, combining (1)–(4), and (6), we can express the magnitude of current under normal condition as

$$\left|\dot{I}_A\right| = \left|\frac{\dot{U}_{AB} + \dot{U}_{BC}}{Z_\Delta}\right| = 3\frac{U_m}{Z_\Delta} \tag{7}$$

and that when T_1 has OCF, the magnitude of the fault current is as follows:

$$\left|\dot{I}_{\text{A\_fault}}\right| = \left|\frac{\dot{U}_{An} + \dot{U}_{Bn}}{Z_\Delta}\right| = \frac{U_m}{Z_\Delta}. \tag{8}$$

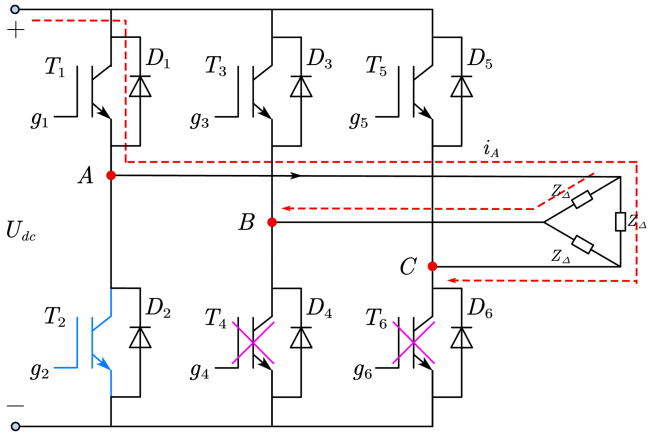

Fig. 6. Phase A current when T_4 and T_6 faulty (i_A).

The ratio of the fault current magnitude to the magnitude of current under normal condition can be expressed as follows:

$$R = \frac{\left|\dot{I}_{\text{A\_fault}}\right|}{\left|\dot{I}_A\right|} = \frac{1}{3}. \tag{9}$$

Thus, when T_1 is in OCF condition, the maximum value (8) of i_A within FDW will be less than one-third of the magnitude (7) of the current under normal conditions. This is the first rationale for designing the three-phase VSI fault diagnosis algorithm.

The above analysis is for fault scenarios (b), Case I. For Cases II, III, and VI, the analysis needs to address scenarios that one of the remaining five switches have OCF with T_1. Fig. 5(a) shows that in these five cases, the effect on the FDW current of T_1 flowing path is negligible. The current will be still less than 1/3 of its normal value. Equation (9) is also applicable to scenarios (b), Case II, Case III, and Case IV.

For scenarios (c), when T_1 is not faulty, during the FDW of T_1, the current i_A is the sum of the current generated by voltage U_{AB} applied on load Z_{AB} and the current generated by voltage U_{AC} applied on load Z_{AC}. However, when both T_4 and T_6 are in OCF condition simultaneously, no current will pass through phase A. The current value characteristic is similar to the scenarios when T_1 in faulty condition, the current i_A decreases significantly.

Fig. 6 depicts the current flow path of scenarios (c) case T_4 and T_6 have OCFs simultaneously. The dashed line in the diagram indicates the normal i_A flowing path. However, due to both T_4 and T_6 being in faulty condition, this path cannot be established, leading to i_A current significantly decreased. Consequently, a zero current mode similar to that due to T_1 OCF is formed.

This suggests that when utilizing a current ratio of less than 1/3 as the fault detection criterion to identify a single switch with OCF in a three-phase VSI, it is crucial to consider fault conditions involving two switches from two different phase legs, both located at either the top or bottom side, experiencing simultaneous faults and to exclude such cases. Table III illustrates the six scenarios of misdiagnosis resulting from simultaneous faults in two switches. This constitutes the second rationale for designing the three-phase VSI fault diagnosis algorithm.

TABLE III
SIX CASES OF TWO SWITCHES HAVING OCF

Affected switch	OCF switches	Affected switch	OCF switches
T_1	T_4T_6	T_2	T_3T_5
T_3	T_2T_6	T_4	T_1T_5
T_5	T_2T_4	T_6	T_1T_3

B. Fault Diagnosis Under Unbalanced Load Current

1) Unbalanced Loads: The above discussion assumes operating conditions where switch OCFs occur with well-balanced loads connected to the VSIs. Abnormal conditions causing load unbalance in practical applications may include: (a) Circuit aging: very severe insulation deterioration and conductor oxidation, in a load motor, could unbalance the load phase impedances, at a level that would affect the diagnosis of inverter faults. This effect would probably be much too severe to permit continued operation. (for example, it could possibly present a fire risk) (b) Partial phase circuits shorting in three-phase equipment, e.g., from shorting turns in machine windings. (c) Load OCFs: One phase of the load becomes open-circuited, resulting in a disruption to the current flow. (d) Load short circuit faults: A load experiencing a phase-to-ground or phase-to-phase short circuit would generally have severely abnormal current waveforms.

Note that a severe current unbalance in a three-phase inverter system, such as in cases (c) and (d), or arising in the inverter, can result in motor vibration severe enough to damage it and other equipment. Such situations would require the complete drive system to be switched OFF. Modest unbalance can also occur in loads that are not inherently balanced but where a useful attempt at equal partitioning has been made. In this work, only minor load unbalance faults are considered, where the system can still operate without the whole system being switched OFF. Equipment losses and electromagnetic interference may remain tolerable, but importantly the accurate detection and location of inverter switch OCFs may be affected. Hence, it is clearly worth considering ways of mitigating the effect of moderate load unbalances on the accuracy of diagnosis of inverter faults.

As described in Section II, for each of the six switches in a VSI, their OCF corresponds to a unique current FDW and the magnitude of this FDW is noted as $I_{m\_T_p}$, (p = 1-6). For example $I_{m\_T_1}$ stands for the magnitude of FDW for switch T_1. For accurate detection of switch fault, a factor, $K_{\text{unbalance}}$ is defined as an indicator for evaluating the level of three-phase current unbalance. It is given as

$$K_{\text{unbalance}} = \frac{1}{6}\sum \frac{\left|I_{\text{avg}} - I_{m\_T_p}\right|}{I_{\text{avg}}} \tag{10}$$

where I_{avg} is the mean average of six current FDW magnitudes, defined as

$$I_{\text{avg}} = \frac{1}{6}\sum_{p=1}^{6}\left|I_{m\_T_p}\right|. \tag{11}$$

During normal operation, $K_{\text{unbalance}}$ is small approaching zero, but a high value of $K_{\text{unbalance}}$ indicates a severe unbalance in the three-phase load. Simulation studies of all OCFs listed in Table I have shown that it is adequate to set a threshold value of 0.1 for $K_{\text{unbalance}}$ to distinguish unbalanced phase currents caused by either switch OCFs or load faults. When $K_{\text{unbalance}} > 0.1$, a switch OCF may have occurred, and the detection procedure can be triggered. If $K_{\text{unbalance}} < 0.1$, it implies the load has minor faults.

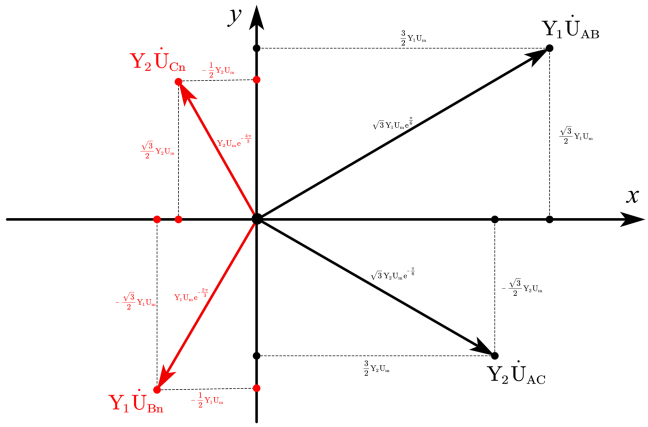

Fig. 7. Numerator and denominator vectors of $R_{\text{unbalance}}$.

In the previous exposition, the ratio of fault current magnitude to current magnitude of a three-phase VSI under normal balanced load condition was described. Similarly, by combining (4) and (6), the ratio under unbalanced load conditions can be obtained as

$$R_{\text{unbalance}} = \left|\frac{\dot{U}_{Bn}}{Z_{AB}} + \frac{\dot{U}_{Cn}}{Z_{AC}}\right| \Big/ \left|\frac{\dot{U}_{AB}}{Z_{AB}} + \frac{\dot{U}_{AC}}{Z_{AC}}\right|. \tag{12}$$

In the equation, by setting $Y_1 = 1/Z_{AB}$, $Y_2 = 1/Z_{AC}$, the numerator and denominator of (12) are the magnitudes of two vectors. Fig. 7 illustrates these vectors. By performing Cartesian coordinate decomposition, vector synthesis, and subsequently calculating their magnitudes, we can obtain

$$R_{\text{unbalance}} = \sqrt{\frac{(Y_1+Y_2)^2 + 3(Y_1-Y_2)^2}{9(Y_1+Y_2)^2 + 3(Y_1-Y_2)^2}}. \tag{13}$$

To analyze the relationship between $R_{\text{unbalance}}$ and Y_1 and Y_2, let the Y_1 and Y_2 vary in the range of 0–10. When the range of variation is 0–1 it indicates an increase in impedance, similar to the unbalanced scenario (a) for circuit aging. $Y_1 = Y_2 = 1$ corresponds to a standard reference load. The variation from 1 to 10 corresponds to a decrease in impedance, similar to the unbalanced scenarios (b) internal component short circuit.

Fig. 8 shows plots of the distribution of $R_{\text{unbalance}}$ values as Y_1 and Y_2 vary. For values of $R_{\text{unbalance}}$ clustered around 0.33, the ratio of Y_1 to Y_2 is close to 1, which indicates a small unbalance. As the unbalance increases, the ratio of Y_1 to Y_2 deviates from the line with a slope of 1, the $R_{\text{unbalance}}$ ratio exceeds 1/3. In the extremely severe unbalanced condition, the $R_{\text{unbalance}}$ even reaches up to 0.58. In summary, in minor unbalanced condition, the ratio of fault current magnitude to the magnitude of current with OCFs remains limited within a range of 1/3. The same current value characteristics also apply to the scenarios of minor load unbalance.

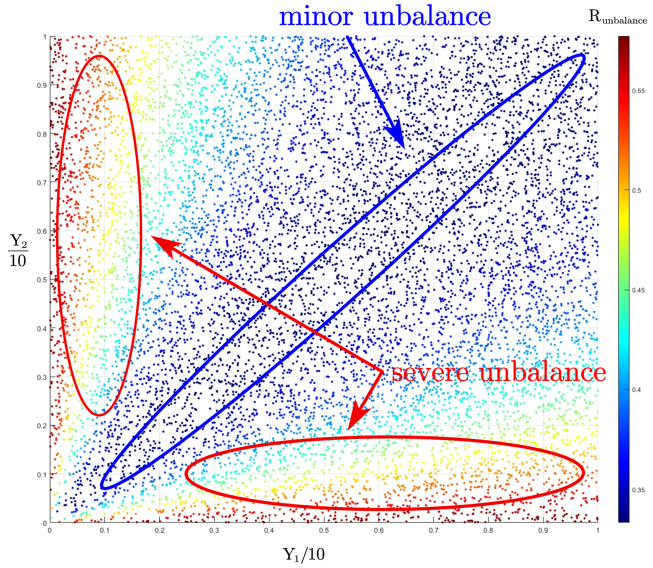

Fig. 8. Numerical distribution plot of $R_{\text{unbalance}}$ (Y_1, Y_2).

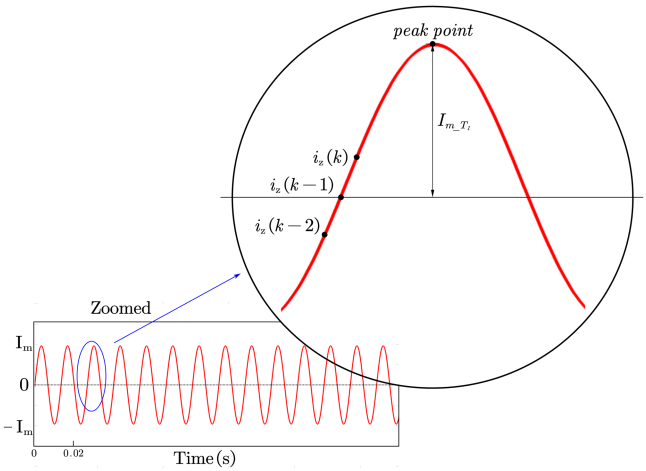

Fig. 9. FDW zero crossing of T_1.

2) Current Normalization for Low Load Cases: A three-phase inverter can be used in many areas, some examples of its application are given as follows: (a) Home appliances such as air conditioners combined with home battery energy storage systems. The three-phase inverters can convert stored dc energy into ac power for driving air conditioners or supplying other household equipment. (b) Electric vehicles for road and rail transportation. Inverters are used to convert the dc battery power to ac form to drive the electric motors pulling electric vehicles and ac tractions. (c) Industrial applications, Inverters are used in industrial machinery, such as motor controllers and variable frequency drives, to control the speed and direction of the machine tools, pumps cooling fans, etc.

Among the aforementioned applications, (a) gives relatively low load changes. However, applications in (b) and (c) areas often present higher levels of load variations. When a motor drive powered by an inverter is running at a light or no load condition, the current drawn by the three-phase inverter decreases sharply and can be typically as low as between 5% and 10% of the rated value.

Under these conditions, if the rated current is still taken as the reference value for current measurement normalization as

$$I_{\text{sample}} = \frac{I_{\text{measured}}}{I_{\text{ref}}} \tag{14}$$

where I_{measured} is the measured phase value, I_{ref} is the $\sqrt{3}$ times rated current of the system. (14) is the ratio similar to (9). Under low or no load conditions, the ratio may become less than 1/3, similar to that of an OCF current ratio, hence causing misdiagnosis. It is necessary to normalize the sampled current using a formula different from (14), namely renormalization.

$$I_{\text{sample\_T}_\text{p}} = \frac{I_{\text{measured}}}{I_{\text{m\_}T_p}} \tag{15}$$

where $I_{\text{m\_}T_p}$ is the monitored magnitude of T_1. Equation (14) is the normalization for normal condition, (15) is applied when the measured current changed significantly due to load reduction. For operation conditions where the load varies greatly, the balance factor of the three-phase inverter load remains basically unchanged, and $K_{\text{unbalance}}$ is lower than the threshold of 0.1. In this case, operating the re-normalization (15) can prevent the misdiagnoses of OCF under low-load situations. The normalization changes in (14) and (15) serve as the sampling rationale for our real-time fault diagnosis algorithm, specifically designed to address load variations.

IV. Fault Diagnosis

A. Location of FDW

As discussed earlier when an OCF occurs in a switch or switches of a VSI, according to (9), (13), (14), and (15), the current values evaluated according to FDW after normalization are lower than 1/3. So, it is crucial to locate the FDWs of each switch to identify whether the related switch has OCF.

Fig. 9 illustrates the FDW zero crossing of T_1, there are two points important to identify whether OCF occurs; the starting point and the peak point. The former is a zero crossing point that indicates the samples after this point enter the FDW of T_1. The peak point is the one having the highest magnitude amongst samples of FDW, and its magnitude is noted as $I_{m\_T_1}$. The criterion for zero crossing point can be identified as

$$\begin{cases} i_{\text{z}(k)} > 0 \\ i_{\text{z}(k)} - i_{z(k-1)} > 0 \\ i_{\text{z}(k-2)} < 0 \end{cases} . \tag{16}$$

Among the three current samples $(i_z(k),\ i_z(k-1)$, and $i_z(k-2)$ at k, k-1 and k-2 points, the one having the smallest absolute value is the zero crossing point.

Taking switch T_1 having OCF as an example, assuming that the starting point is detected, every sample after one cycle number will be the starting point of FDW. The cycle number

TABLE IV
FAULT DETECTION SAMPLES FOR SIX SWITCH

Switch	Number range	Switch	Number range
T_1	$[0\ N_0/2]$	T_2	$[N_0/2\ N_0]$
T_3	$[N_0/3\ 5N_0/6]$	T_4	$[5N_0/6\ 4N_0/3]$
T_5	$[2N_0/3\ 7N_0/6]$	T_6	$[0\ 2N_0/3]$

N_0 is defined as

$$N_0 = T_0 \times f_0 \tag{17}$$

where T_0 is the period of the inverter current, and f_0 is the sampling frequency of the current sensor.

After locating the starting point, the measured current samples are numerically labeled from 0 to $2N_0$. When the number exceeds $2N_0$ it is reset to 0 and the counting is resumed. For T_1 having OCF, the current in phase A assumed to be the FDW of T_1 at a quarter of a cycle (5 ms) after zero crossing. Consequently, every current sample from 0 to $N_0/2$ is within the T_1 FDW range. Due to the phase difference of 120° between the three-phase currents, the starting point of T_1 can be used to obtain the fault detection samples of the six switches. Table IV shows the number for each switch.

After locating the FDWs, we evaluate the magnitudes of six switches' $I_{m\_T_p}$ (p = 1-6) which are the peak point of the FDWs, Take switch T_1 as an example

$$\mathrm{I}_{\mathrm{m\_}T_1} = I_{N_0/4} \tag{18}$$

The same calculation is applied to the other five switches. Therefore, the time taken for $K_{\mathrm{unbalance}}$ for evaluating all six magnitudes is 5/6 T_0.

B. Fault Diagnosis Method

Under normal conditions, only a small portion of current values within the FDW exhibits ratios to the magnitude lower than 1/3. However, when the corresponding switch experiences an OCF, almost all the current samples within FDW have their ratios below 1/3. Therefore, faults can be detected by statistically analyzing the number of samples with ratios below 1/3. The number counting for the faulty samples is defined as

$$N_C = \begin{cases} N_C + 1 & if\ I_{\mathrm{sample}} \geqslant 1/3 \\ N_C & if\ I_{\mathrm{sample}} < 1/3 \end{cases}. \tag{19}$$

When a fault occurs, the count of sampling points is increased to $N_0/2$, the value of N_C will be close to $N_0/2$. Therefore, the fault detection function is defined as

$$\mathrm{F}_{\mathrm{detection}} = \begin{cases} 1 & if\ \frac{2N_C}{N_0} \geqslant 1 \\ 0 & if\ \frac{2N_C}{N_0} < 1 \end{cases} \tag{20}$$

where $F_{\mathrm{detection}} = 1$, indicates that the detected switch experiences an OCF.

Finally, we consider the cases when two switches are faulty simultaneously, as listed in Table III. Fig. 10 shows the flowchart of the diagnosis method. The method consists of the following three main steps.

a) Sample processing: Initially current samples of the three-phase VSI are taken and normalized (14). Then the starting points of the six switches' FDWs are searched by detecting their zero crossing points (16) when the system is running normally and stably. Periodically normalize the received samples and locate samples within the FDWs of six switches by referring to Table IV.

b) Loads estimation: This step detects the magnitudes of FDWs for six switches, these are the middle points of each FDWs current values, for a detailed explanation, one can refer to (18). Once this is done unbalance parameters $K_{\mathrm{unbalance}}$ can be calculated by substituting the magnitude ($I_{m\_T_1}$–$I_{m\_T_6}$) into (11). Then, determine whether re-normalization processing is necessary according to $K_{\mathrm{unbalance}}$ value. If the value of the $K_{\mathrm{unbalance}}$ is greater than the threshold, renormalization is not required, and if the value of the $K_{\mathrm{unbalance}}$ is lower than the threshold, operate the renormalization processing by (15).

c) Fault detection: Use (19) to statistically calculate the faulty current value number (ratio lower than 1/3) of the FDWs samples. The faulty counting number N_C is obtained and substituted into the fault detection function (20) to obtain the decision of fault result. Finally, check whether this

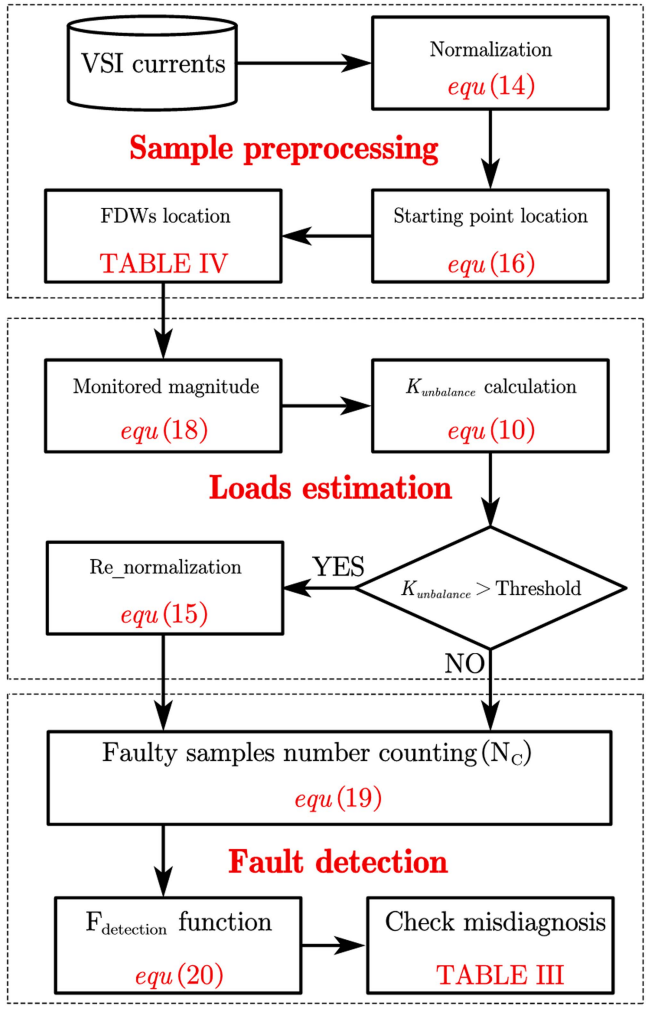

Fig. 10. Flowchart of fault diagnosis method.

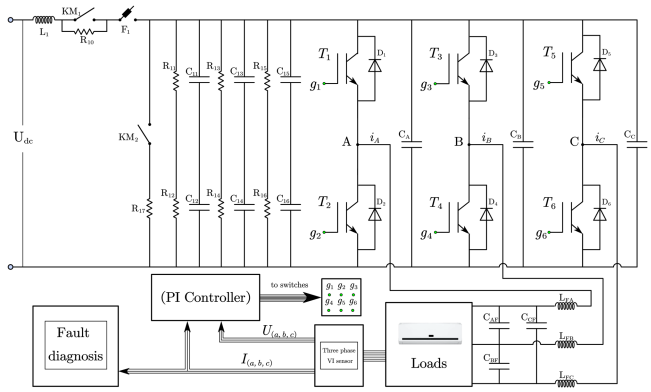

Fig. 11. Air-conditioning inverter schematic for a 25 T train.

fault detection result is three switches OCF caused by other dual-switch faults as indicated in Table III. If not, the diagnosis of the fault occurring in the corresponding switch is established. If yes, the fault result is deemed invalid.

Taking into account the time for clearing the misdiagnosis fault result, it is beneficial to enhance the robustness of the proposed method by setting the last and definitive result of the fault diagnosis if the fault detection persists for two cycles.

V. Simulation

To validate the OCF detection method, the MATLAB Simulink package is used, and the simulated inverter-driven system is an air-conditioner used in a 25-ton train. In these simulations, fault inception times were randomly selected, with different times determining fault inception angles. Through the above analysis, it is evident that the most complex scenarios encompass two switches from two different phase legs, positioned either at the top or bottom side, simultaneously experiencing faults. Consequently, the corresponding experiments were conducted under unbalanced conditions and load variations.

Fig. 11 illustrates the schematic of the inverter system. L_1, R_{10}, KM_1, and F_1 are components of the DC-source side switch snubber circuit, while KM_2 and R_{17} form the discharge circuit for releasing stored energy in the supporting capacitor after the inverter stops. The dc-side support capacitor comprises C_{11}–R_{16} and resistors R_{11}–R_{16}. T_1–T_6 represent the IGBTs, D_1–D_6 are the freewheeling diodes for their corresponding switches. The inverter output terminals to the load have *L–C* filters which are denoted as L_{AF}–C_{AF}, L_{BF}–C_{BF}, and L_{CF}–C_{CF}, respectively. In addition, there are capacitors labeled as C_A, C_B, and C_C for eliminating dc-bus voltage ripples. A PI current controller is used with hysteresis for each phase. The main simulation parameters are provided in Table V.

Fig. 12 shows four different cases of OCFs which all have switch T_1 being faulty. Fig. 12(a) is a single T_1 OCF (Case I), the FDW for T_1 is located in the positive half wave of phase A. The fault in T_1 occurs at 0.215 s. As the fault emerges later in the first FDW, it remains undetected. However, in the subsequent FDW following the fault, The current values within the FDW are all below 1/3, so the OCF is confirmed. The time duration for detecting this fault is 27 ms.

Fig. 12(b) and (c) shows the FDW for T_1&T_2 simultaneously faulty (Case II). Fig. 12(b) depicts the fault occurring at 0.198 s. The T_1 fault is detected in the second FDW after the fault, the time for T_1 fault detected is 24 ms. Fig. 12(c) locates the T_1 FDW in phase A. In the first FDW where the fault occurs, all current values within the FDW are below 1/3. The time required to detect the T_2 fault is 14 ms.

Fig. 12(d) and (e) shows T_1&T_4 having OCF (Case III). The time for both switches having OCF was 0.222 s. Fig. 12(d) located T_1 FDW from 0.22 s to 0.23 s in phase A, it took 8 ms to detect the T_1 OCF. For T_4, Fig. 12(e) locates T_4 FDW from

TABLE V
Main Parameters of Simulation Model

Parameters	Symbol	Value
DC voltage	U_{dc}	600 V
AC voltage	U_{ac}	380 V
Frequency of current	f	50 Hz
Switching frequency	f_s	3 kHz
Suport resistor	$R_{(11-16)}$	33 kΩ
Suport capacitor	$C_{(11-16)}$	6.8 mF
Filter inductors	$L_{(AF,BF,CF)}$	4.5 mH
Filter capacitors	$C_{(AF,BF,CF)}$	90 nF
Capacitors	$C_{(A,B,C)}$	1.2 nF
Active power	P	35 kW
Reactive power	Q	16.9 kW

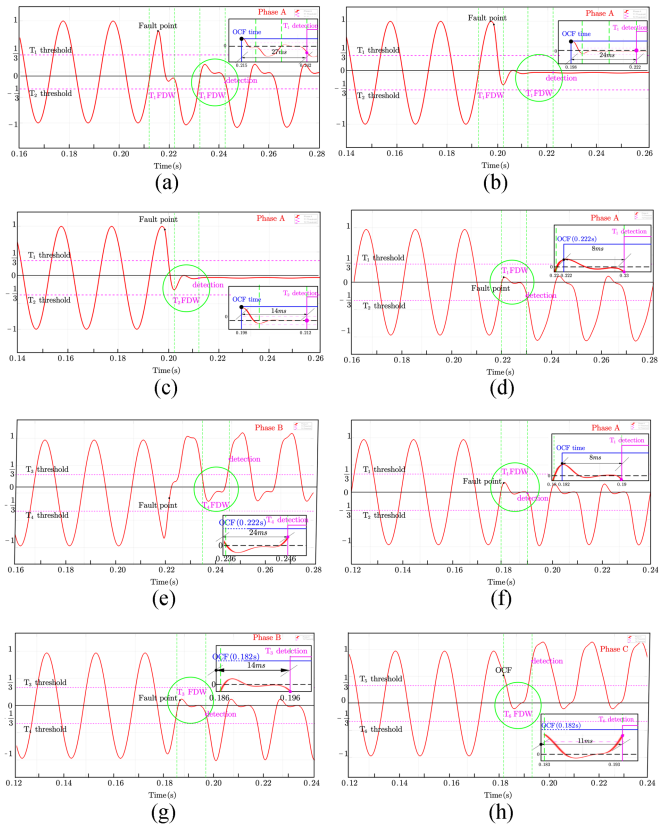

Fig. 12. Fault diagnosis simulation for T_1 OCF in balance loads.

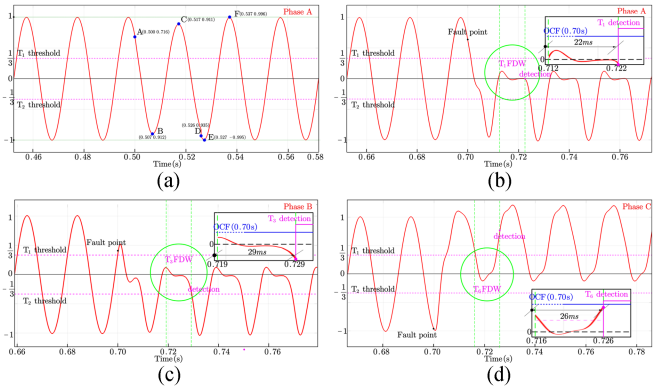

Fig. 13. Fault diagnosis simulation for T_1&T_3 OCFs in unbalance loads.

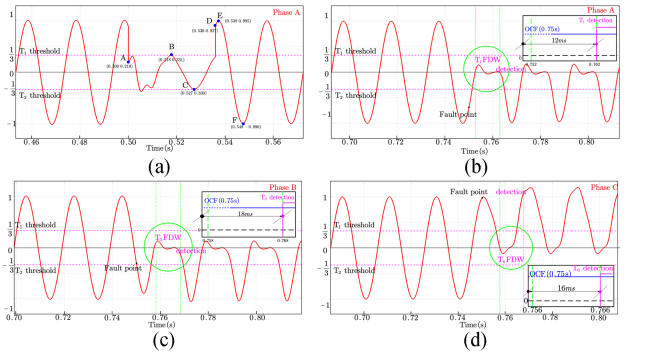

Fig. 14. Fault diagnosis simulation for T_1&T_3 OCFs when loads change rapidly.

0.236 s to 0.246 s in phase B, the current values within the FDW are all below 1/3, at the end of FDW the OCF of T_4 was detected. The time for fault to be detected is 24 ms

Fig. 12(f)–(h) shows both T_1&T_3 having OCF (Case IV). The occurrence for OCF on both switches was 0.182 s. Fig. 12(f) shows T_1 FDW from 0.18 s to 0.19 s in phase A, it takes 8 ms to detect the T_1 having OCF. For T_3, Fig. 12(c) locates FDW from 0.186 s to 0.196 s in phase B, the current values within the FDW are all below 1/3, and at the end of FDW, the OCF of T_3 is detected. The time taken for detecting this fault is 14 ms.

Note that in this case T_6 is also affected by OCF on T_1&T_3. Fig. 12(h) shows that FDW of T_6 from 0.183 s to 0.193 s. At the time instant 0.196 s the detection algorithm obtains the result that there are 3 switches in OCF condition. According to Table IV, we exclude the assumption that an OCF occurs in T_6 and obtain the result that only T_1 and T_3 have OCFs.

From the above simulation results, we can conclude that the proposed detection method is capable of diagnosing inverter switch OCFs and the time taken for diagnosis is less than 2 fundamental sinusoidal periods.

To test the method for diagnosing OCFs under minor unbalanced loads, the simulation is set to emulate the condition of circuit aging hence the phase A impedance becomes higher than normal, leading to a lower phase current. In this case, assuming T_1 and T_3 have OCFs simultaneously, making the operation under the most complex scenario (Case IV).

Fig. 13(b)–(d) shows the diagnosis of T_1 and T_3 OCFs. Fig. 13(b) shows that the current values were all below 1/3 with the FDW of T_1. The fault detection time is 22 ms. Fig. 13(c) shows that the current values were all below 1/3 with FDW of T_3. The fault detection time is 29 ms. Fig. 13(d) shows that the current values were all below 1/3 with the FDW of T_6. The fault detection time is 26 ms. So the whole detection time is 29 ms and according to Table III, the detection result is T_1&T_3 OCFs and the detection is workable for minor unbalanced loads.

Fig. 14 shows the T_1&T_3 OCFs simultaneously. Fig. 14(a) shows the loads power drops significantly at 0.50 s (point A), the magnitude $I_{m\_T_1}$ becomes 0.331 (point B) and $I_{m\_T_2}$ becomes 0.330 (point C). The diagnosis model monitors the changes and makes a renormalization at point D, the magnitude $I_{m\_T_1}$ and $I_{m\_T_2}$ all become 1, which can be seen from points E and F.

TABLE VI
MAIN PARAMETERS OF THE EXPERIMENTAL SETUP

Parameters	Symbol	Value
DC link voltage	V_{dc}	500 V
Filter inductances	$L_aL_bL_c$	1.1 mH
Filter Capacitors	$C_aC_bC_c$	50 uF
Sample period	T_{sample}	5 ms
Motor Rated power	U_{RMS}	7.5 kW
Motor voltage (fundamental RMS)	U_{RMS}	380 V
Motor current (fundamental RMS)	I_{RMS}	15.4 A
Rated speed	n	1460rpm(continuous)
Power factor	$\cos\varphi$	0.86
Rated frequency	f	50.0 Hz
Rated torque	T_e	48.96 Nm
Efficiency	η	0.93
Motor poles	p	4

Fig. 14(b)–(d) shows the diagnosis of T_1 and T_3 OCFs. Fig. 14(b) shows that the current values were all below 1/3 with the FDW of T_1. The fault detection time is 12 ms. Fig. 14(c) shows that the current values were all below 1/3 with the FDW of T_3. The fault detection time is 18 ms. Fig. 14(d) shows that the current values were all below 1/3 with the FDW of T_6. The fault detection time is 16 ms. So the whole detection time is 18 ms and according to the exclusion rule of Table III, the detection result is T_1 and T_3 OCFs and the detection method is suitable for the loads rapidly changing situation.

To verify the robustness of the proposed algorithm to parameter variations, a series of experiments were conducted on this simulation platform. The results are presented in Table VIII at the end of the article. The table illustrates that when the parameter is $K_{\text{unbalance}}$ in the range of 0–0.15, the error is minimal. However, as the unbalanced parameter increases, errors begin to manifest. With $K_{\text{unbalance}}$=0.30, the system becomes highly unbalanced, resulting in a diagnostic error as high as 1.2%. In contrast, variations in the load have a relatively minor impact. Even with a 60% load variation, the error remains at only 0.2%.

VI. EXPERIMENT VERIFICATION

A. Result Analysis

An experimental platform, as shown in Fig. 15, has been established to validate the proposed fault diagnosis method. The

TABLE VII
COMPARISON WITH OTHER FAULT DIAGNOSIS METHODS

Ref	Diagnosis method	Diagnosis time	Faults types	Calculation burden	Loads adaptability	Robustness
[18]	Voltage based	—	6	low	high	high
[19]	Voltage based	0.02s	21	low	low	low
[20]	Voltage based	0.04s	21	low	low	low
[21]	Voltage based	—	6	low	low	low
[22]	Current based	0.07s	21	low	low	moderate
[23]	Current based	—	12	low	low	low
[24]	Current based	0.04s	21	low	moderate	moderate
[25]	Current based	1.30s	21	moderate	—	high
[26]	Current based	0.002s	6	low	low	low
[27]	Model based	0.04s	21	moderate	low	moderate
[28]	Model based	0.01s	6	moderate	low	low
[29]	Model based	0.01s	—	moderate	low	moderate
[30]	Intelligent technologies	—	6	high	moderate	moderate
[31]	Intelligent technologies	0.06s	—	high	moderate	moderate
[32]	Intelligent technologies	—	—	high	moderate	high
This paper	The proposed method	0.04s	21	low	high	high

TABLE VIII
DIAGNOSTIC ERRORS UNDER VARIOUS UNBALANCE PARAMETERS AND LOAD VARIATION

$K_{\text{unbalance}}$	Error	$K_{\text{unbalance}}$	Error	Loads variation(%)	Error	Loads variation(%)	Error
0.05	0.0%	0.20	0.3%	10	0.0%	40	0.0%
0.10	0.0%	0.25	0.4%	20	0.0%	50	0.1%
0.15	0.1%	0.30	1.2%	30	0.0%	60	0.2%

Fig. 15. Experimental setup.

setup includes an IGBT three-phase inverter cabinet, associated hardware equipment, a dSPACE system (comprising DS1007, DS2002 A/D Board, DS4004I/O Board), and software tools for control, communication, and fault diagnosis algorithm model. The inverter cabinet contains power devices, current sensors, and interfaces with the dSPACE system for real-time communication. The dSPACE Control Desk software allows for real-time monitoring of collected signals and parameter adjustments. The main parameters of the inverter drive system are provided in Table VI.

It is worth noting that the previous simulation involved a complex and realistic three-phase inverter system, confirming the method's efficacy with closed-loop inductance loads. However, in practical engineering applications, the load is typically a motor load. Thus, this experimental validation complements the applicable verification.

1) Normal Operation at Rated Load: This experiment covers all fault types listed in Table I, including Cases I–IV. To validate the practical applicability of the proposed method in engineering, the timing of all faults is set randomly. Fig. 16 illustrates the experimental results of a three-phase inverter subjected to four distinct types of fault for T_1. Fig. 16(a) depicts a single T_1 OCF (CASE I), with a diagnostic response obtained 10 ms after the fault occurrence. OCFs occurring on T_1 and T_2, (CASE II), are presented in Fig. 16(b) and (c). The diagnosis for T_1 is observed at 18.3 ms after the fault, while the diagnosis for T_2 is detected at 28.2 ms after the fault in Fig. 16(b) and (c), respectively. Fig. 16(d) and (e) showcases T_1 and T_4, respectively, representing fault occurrences in different phases and sides of the inverter (CASE III). The detection of T_1 fault occurs 28 ms after the fault in Fig. 16(d), while in Fig. 16(e), T_1 fault detection happens at 11.0 ms after the fault. Furthermore, Fig. 16(f), (g), and (h) exhibit the OCFs of T_1 and T_3, representing a double fault in different phases but on the same top side of the inverter (CASE IV). The detection of T_1 fault occurs 18.0 ms after the fault in Fig. 16(f), T_3 fault detection happens 10 ms after the fault in Fig. 16(g). Fig. 16(g) and (h) illustrates the false detection

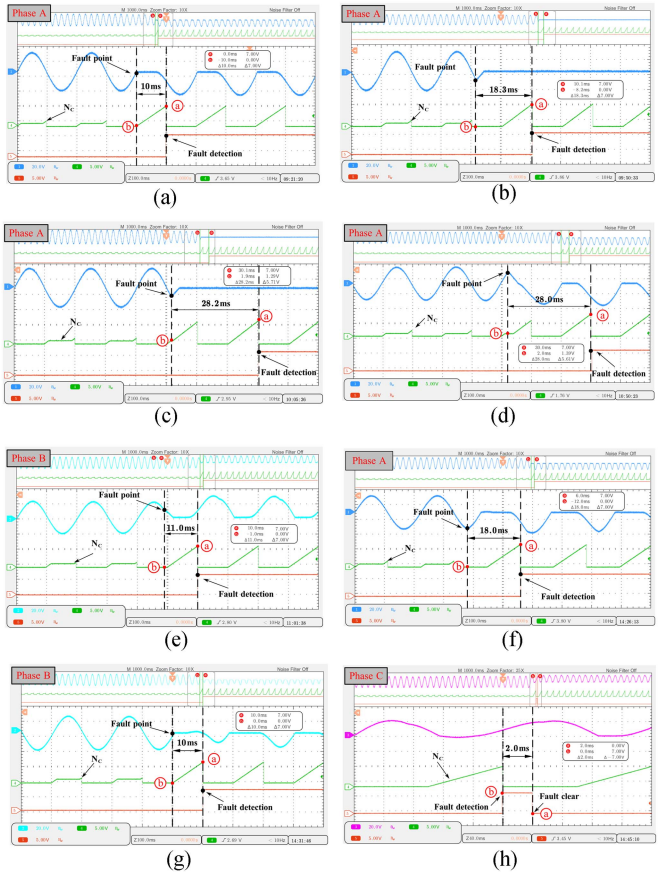

Fig. 16. Experimental results in rated loads.

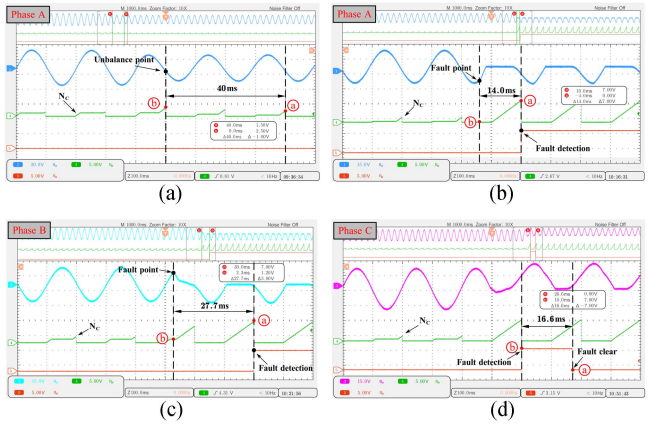

Fig. 17. Experimental results with light unbalanced loads.

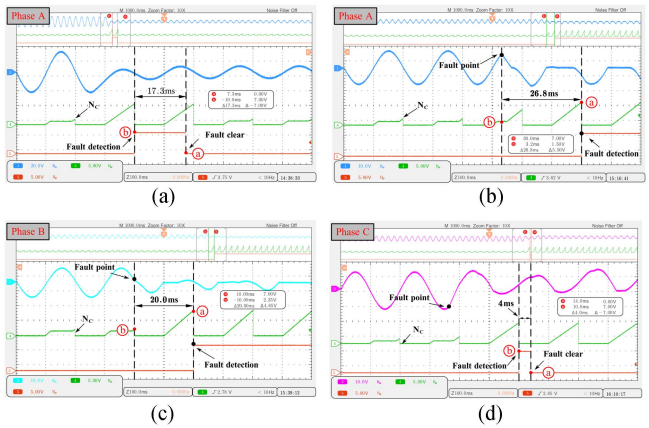

Fig. 18. Experimental results with rapid changing loads.

of T_6 fault followed by a clear signal 2.0 ms later. All faults are accurately detected, with the longest diagnostic time being 28.2 ms. The proposed method showcases its speed and accuracy in real-time diagnostics for all four fault types.

2) VSI Operation With Unbalanced Loads: In order to evaluate the performance of the proposed fault diagnosis method under light unbalanced load conditions by adding a 10 Ω resistance in phase A. The most complex fault scenario (CASE IV) was examined. This scenario involves OCFs of T_1 and T_3 occurring in different phases but on the same top side of the inverter with random timing for the faults. Fig. 17(a) illustrates the variation of the number counting (N_C) of T_1 after the occurrence of light load unbalanced conditions. Following renormalization, the N_C value remains consistent with the value observed under balanced conditions. Fig. 17(b) shows the detection of the fault at 14.0 ms after the occurrence of T_1 OCF. Fig. 17(c) demonstrates the fault detection at 27.7 ms after the occurrence of T_1 OCF. Fig. 17(d) displays the misdiagnosis of T_6 fault followed by a clear signal at 16.6 ms later. This experiment validates the effectiveness of the proposed renormalization step in handling minor load unbalances and enabling the successful diagnosis of complex fault scenarios (CASE IV).

3) VSI Operation With Rapid Changing Loads: Experimental test was conducted to validate the application for rapidly changing load conditions where the load abruptly drops to 20%. Specifically, the most complex fault scenario (CASE IV) was investigated, involving OCFs in T_1 and T_3 with random timing. Fig. 18(a) illustrates the variation of the number counting (N_C) of T_1 following intense load fluctuations. Initially, a sudden decrease in current values led to a misdiagnosis for T_1. However, after renormalization, the fault result cleared after 17.3 ms, and the N_C value remained consistent with the rated conditions. Fig. 18(b) demonstrates the detection of the fault 26.8 ms after the occurrence of T_1 OCF. Fig. 18(c) displays the fault detection 20.0 ms after the occurrence of T_3 OCF. Fig. 18(d) reveals the misdiagnosis of T_6 fault followed by a clear signal 4.0 ms later. The impact of rapid load variations was promptly mitigated by the renormalization step. For T_1 and T_3 faults (Case IV), precise localization was achieved 27.7 ms after the fault occurrence.

In summary, the experimental results confirm that the diagnosis time is below 40 ms (2 cycle times), and the real-time diagnosis method effectively achieves accurate fault detection for three-phase VSIs through straightforward current sample processing. Furthermore, the method demonstrates robustness for load variation.

B. Comparison Between the Fault Diagnosis Method

Table VII summarizes the characteristics of fault diagnosis methods for three-phase inverters. The table provides a comprehensive analysis of fault diagnosis time, types of faults identified,

computational requirements, adaptability to load variations, and robustness. The characteristics of the proposed fault diagnosis method in this article are listed at the bottom of the table.

Voltage-based methods [18], [19], [20], [21] have low computational requirements. However, due to the high complexity of voltage for double-switch OCFs, the fault types addressed in [18] and [21] are limited to single-switch OCFs. In addition, these methods exhibit weak adaptability to load variations.

Current-based methods [22], [23], [24] can achieve fault diagnosis within a shorter time frame. However, these three methods exhibit poor robustness due to strong dependence on the standard current model. Method [26] demonstrates good robustness but sacrifices diagnosis time, resulting in a longer diagnosis time of up to 1.3 s.

Model-based methods [27], [28], [29] offer fast diagnostic capabilities but require meticulous handling of the constructed model, thus demanding computational support. They exhibit moderate adaptability to load variations and robustness, making them a balanced diagnostic approach.

Intelligent technology-based methods [30], [31], [32] leverage intelligent technologies such as neural networks for fault diagnosis through feature extraction. On one hand, implementing intelligent technologies requires high equipment requirements and high computational support. On the other hand, the current methods lack sufficient consideration for load variations, and the establishment of databases relies on simulation. However, they hold the potential for improved robustness.

Compared to these methods, the proposed method demonstrates rapid fault detection and location, achieving it within 0.04 s (two fundamental circles). It efficiently handles all 21 types of faults with low computational burden and high accuracy. Notably, this is a highly straightforward real-time fault diagnosis method, relying only on current sampling, processing and subsequent determinations. However, it emphasizes showcasing innovations, especially in the analysis of current variations during OCFs. It is crucial when dealing with currents caused by double switch OCFs on the inverter's same top or bottom side (see Fig. 6). This refined analysis enhances accuracy in OCF current assessment and effectively addresses the issue of misdiagnosis seen in previous current-centric diagnostic methods. Furthermore, the proposed current normalization technique introduces a transformative concept, the unbalanced factor, beyond accounting for current amplitude changes. This innovative addition helps mitigate the disruptive effects of load fluctuations on OCF diagnosis. This adaptable normalization approach significantly boosts the flexibility and effectiveness of fault diagnosis methods, especially in dynamic load conditions. The method's effectiveness is evident in its ability to handle minor load unbalances and sudden fluctuations adeptly. This robustness enhances the practical applicability and reliability of the method.

VII. Conclusion

This article has developed a current analysis method for three-phase VSIs having switch OCFs. The method could identify the abnormal patterns of the current waves, known as FDWs, due to the switch OCFs, promptly. Continuously analyzing the FDW starting and peak values greatly enhances the robustness of current-based fault diagnosis for three-phase VSIs. Furthermore, the incorporation of an unbalanced ratio judgment and re-normalization in the method enabled it to handle complex load variations during fault diagnosis. The effectiveness of the proposed method has been validated through both simulation and real experimental tests. The results have shown that the proposed fault diagnosis method can quickly and accurately diagnose single-switch and double-switch OCFs in three-phase VSIs. The diagnosis results for faults under load changes and load unbalanced conditions highlight the method's high robustness in handling load variations.

References

[1] M. R. Miveh, M. F. Rahmat, A. A. Ghadimi, and M. W. Mustafa, "Control techniques for three-phase four-leg voltage source inverters in autonomous microgrids: A review," *Renewable Sustain. Energy Rev.*, vol. 54, pp. 1592–1610, 2016.

[2] H. Chen and H. Zhao, "Review on pulse-width modulation strategies for common-mode voltage reduction in three-phase voltage-source inverters," *IET Power Electron.*, vol. 9, no. 14, pp. 2611–2620, 2016.

[3] J. Chen, D. Sha, J. Zhang, and X. Liao, "An SIC MOSFET based three-phase ZVS inverter employing variable switching frequency space vector PWM control," *IEEE Trans. Power Electron.*, vol. 34, no. 7, pp. 6320–6331, Jul. 2019.

[4] Y. Wang, Z. Li, M. Xu, and H. Ma, "A comparative study of two diagnostic methods based on the switching voltage pattern for IGBT open-circuit faults in voltage-source inverters," *J. Power Electron.*, vol. 16, no. 3, pp. 1087–1096, 2016.

[5] J. Xu, J. Han, Y. Wang, M. Ali, and H. Tang, "High-frequency sic three-phase VSIS with common-mode voltage reduction and improved performance using novel tri-state PWM method," *IEEE Trans. Power Electron.*, vol. 34, no. 2, pp. 1809–1822, Feb. 2019.

[6] H. Yuruk, O. Keysan, and B. Ulutas, "Comparison of the effects of nonlinearities for Si MOSFET and GAN E-HEMT based VSIS," *IEEE Trans. Ind. Electron.*, vol. 68, no. 7, pp. 5606–5615, Jul. 2021.

[7] S. Karimi, P. Poure, and S. Saadate, "Fast power switch failure detection for fault tolerant voltage source inverters using FPGA," *IET Power Electron.*, vol. 2, no. 4, pp. 346–354, 2009.

[8] S. Kwak and J.-C. Park, "Predictive control method with future zero-sequence voltage to reduce switching losses in three-phase voltage source inverters," *IEEE Trans. Power Electron.*, vol. 30, no. 3, pp. 1558–1566, Mar. 2015.

[9] M. Yaghoubi, J. S. Moghani, N. Noroozi, and M. R. Zolghadri, "IGBT open-circuit fault diagnosis in a quasi-z-source inverter," *IEEE Trans. Ind. Electron.*, vol. 66, no. 4, pp. 2847–2856, Apr. 2019.

[10] O. Dieterle, T. Greiner, and P. Heidrich, "Control of a PMSM with quadruple three-phase star-connected windings under inverter short-circuit fault," *IEEE Trans. Ind. Electron.*, vol. 66, no. 1, pp. 685–695, Jan. 2019.

[11] D. Espinoza-Trejo, D. Campos-Delgado, E. Barcenas, and F. Martínez-Lopez, "Robust fault diagnosis scheme for open-circuit faults in voltage source inverters feeding induction motors by using non-linear proportional-integral observers," *IET Power Electron.*, vol. 5, no. 7, pp. 1204–1216, 2012.

[12] I. Jlassi, J. O. Estima, S. K. El Khil, N. M. Bellaaj, and A. J. M. Cardoso, "A robust observer-based method for IGBTs and current sensors fault diagnosis in voltage-source inverters of PMSM drives," *IEEE Trans. Ind. Appl.*, vol. 53, no. 3, pp. 2894–2905, May/Jun. 2017.

[13] F. Wu, Y. Hao, J. Zhao, and Y. Liu, "Current similarity based open-circuit fault diagnosis for induction motor drives with discrete wavelet transform," *Microelectron. Rel.*, vol. 75, pp. 309–316, 2017.

[14] S. Lee, F. Chen, T. M. Jahns, and B. Sarlioglu, "Review on switching device fault, protection, and fault-tolerant topologies of current source inverter," in *Proc. IEEE 13th Int. Symp. Diagn. Elect. Mach., Power Electron. Drives*, 2021, vol. 1, pp. 489–495.

[15] M. T. Fard, J. He, and Z. Wang, "Fault diagnosis and fault-tolerant operation of current source inverter for safety-critical applications," in *Proc. IEEE Transp. Electrific. Conf. Expo*, 2020, pp. 925–929.

[16] B. Jiang and Q. An, "A novel diagnostic technique for open-switch faults of inverters based on operating mode analysis," in *Zhongguo Dianji Gongcheng Xuebao (Proc. Chin. Soc. Elect. Eng.)*, vol. 32, pp. 30–37, 2012.
[17] Q. Wang, Y. Wang, Z. Zhang, and Z. Song, "A diagnosis method for inverter open-circuit faults of brushless DC motor driver systems," *Proc. Chin. Soc. Elect. Eng.*, vol. 33, no. 24, pp. 114–122, 2013.
[18] C. Shu, C. Ya-Ting, Y. Tian-Jian, and W. Xun, "A novel diagnostic technique for open-circuited faults of inverters based on output line-to-line voltage model," *IEEE Trans. Ind. Electron.*, vol. 63, no. 7, pp. 4412–4421, Jul. 2016.
[19] X. Wu, T.-F. Chen, S. Cheng, T. Yu, C. Xiang, and K. Li, "A noninvasive and robust diagnostic method for open-circuit faults of three-level inverters," *IEEE Access*, vol. 7, pp. 2006–2016, 2018.
[20] X. Xu and F. Yu, "A switch open-circuit fault diagnosis method for three-phase inverters based on voltage patterns," in *Proc. 2nd Int. Conf. Elect. Eng. Control Sci.*, 2022, pp. 901–908.
[21] Y. Li, X. Cheng, Z. Yang, Z. Huang, and M. Ke, "Inverter fault diagnosis algorithm based on midpoint voltage deviation polarity and topology reconstruction," in *Proc. IEEE 3rd Int. Conf. Power, Electron. Comput. Appl.*, 2023, pp. 62–67.
[22] H. Yan, Y. Xu, J. Zou, Y. Fang, and F. Cai, "A novel open-circuit fault diagnosis method for voltage source inverters with a single current sensor," *IEEE Trans. Power Electron.*, vol. 33, no. 10, pp. 8775–8786, Oct. 2018.
[23] Z. Jian-Jian, C. Yong, C. Zhang-Yong, and Z. Anjian, "Open-switch fault diagnosis method in voltage-source inverters based on phase currents," *IEEE Access*, vol. 7, pp. 63619–63625, 2019.
[24] K. Li, S. Cheng, T. Yu, X. Wu, C. Xiang, and A. Bilal, "An on-line multiple open-circuit fault diagnostic technique for railway vehicle air-conditioning inverters," *IEEE Trans. Veh. Technol.*, vol. 69, no. 7, pp. 7026–7039, Jul. 2020.
[25] Y. Zhou, J. Zhao, Y. Song, J. Sun, H. Fu, and M. Chu, "A seasonal–trend-decomposition-based voltage-source-inverter open-circuit fault diagnosis method," *IEEE Trans. Power Electron.*, vol. 37, no. 12, pp. 15517–15527, Dec. 2022.
[26] Z. Li et al., "A fast diagnosis method for both IGBT faults and current sensor faults in grid-tied three-phase inverters with two current sensors," *IEEE Trans. Power Electron.*, vol. 35, no. 5, pp. 5267–5278, May 2020.
[27] Z. Li, H. Ma, Z. Bai, Y. Wang, and B. Wang, "Fast transistor open-circuit faults diagnosis in grid-tied three-phase vsis based on average bridge arm pole-to-pole voltages and error-adaptive thresholds," *IEEE Trans. Power Electron.*, vol. 33, no. 9, pp. 8040–8051, Sep. 2018.
[28] Z. Huang and Z. Wang, "A fault diagnosis algorithm for microgrid three-phase inverter based on trend relationship of adjacent fold lines," *IEEE Trans. Ind. Informat.*, vol. 16, no. 1, pp. 267–276, Jan. 2020.
[29] W. Zhang and Y. He, "A hypothesis method for t-type three-level inverters open-circuit fault diagnosis based on output phase voltage model," *IEEE Trans. Power Electron.*, vol. 37, no. 8, pp. 9718–9732, Aug. 2022.
[30] S. Zhang, R. Wang, Y. Si, and L. Wang, "An improved convolutional neural network for three-phase inverter fault diagnosis," *IEEE Trans. Instrum. Meas.*, vol. 71, 2022, Art. no. 3510915.
[31] Y. Xia and Y. Xu, "A transferrable data-driven method for IGBT open-circuit fault diagnosis in three-phase inverters," *IEEE Trans. Power Electron.*, vol. 36, no. 12, pp. 13478–13488, Dec. 2021.
[32] Y. Si, R. Wang, S. Zhang, W. Zhou, A. Lin, and Y. Wang, "Fault diagnosis based on attention collaborative LSTM networks for NPC three-level inverters," *IEEE Trans. Instrum. Meas.*, vol. 71, 2022, Art. no. 3512416.

Yu Luo received the B.E. degree in electrical automation, the M.S. degree in electrical engineering from the Changsha University of Science and Technology, Changsha, China, in 2013 and 2016, respectively, and the Ph.D. degree in traffic equipment and information engineering from Central South University, Changsha, in 2024. His research interests include fault diagnosis and fault tolerant control of power electronic converters, train control, and traction electric drive.

His research interests include fault diagnosis and fault tolerant control of power electronic converters, train control and traction electric drive.

Li Zhang (Senior Member, IEEE) received the Ph.D. degree from Oxford University, Oxford, U.K.

She was then a Lecturer with the University of Bradford and is currently a Senior Lecturer with the School of Electronic and Electrical Engineering, University of Leeds, U.K.

Dr. Zhang is an Adjunct Professor with Chongqing University, China from 2006 till now and Joint Grant holder of China State Natural Science Foundation Fund (60712,201401-2017 12) entitled: Analysis and research on the hot spot effect and it's control method of photovoltaic system. She was a Research Fellow with Oxford University, U.K. She is an Associate Editor for IEEE TRANSACTIONS ON POWER ELECTRONICS and has also been the Associate Editor for the IET proceedings on Power Electronics between 2014 to 2017. She has authored and coauthored three books on power converter circuits and wind power electricity generation. She has authored and coauthored more than 130 technical papers in the fields of power electronics, renewable power generation system and wind generator control.

Chunyang Chen was born in Nanling, China, in 1962. He received the B.E. degree in electric locomotive from Southwest Jiaotong University, Chengdu, China, the Master degree from Hunan University, Changsha, China, and the Ph.D. degree from Beijing Jiaotong University, Beijing, China.

He used to be the Deputy Director of Science and Technology Department of the Ministry of Railways, and the President of Southwest Jiaotong University. He currently serves as the Vice President of Central South University. His research interests include the electric locomotive and intelligent transportation system.

Kang Li (Senior Member, IEEE) received the B.Sc. degree in industrial automation from Xiangtan University, Hunan, China, in 1989, the M.Sc. degree in control theory and applications from Harbin Institute of Technology, Harbin, China, in 1992, and the Ph.D. degree in control theory and applications from Shanghai Jiaotong University, Shanghai, China, in 1995. He also received the D.Sc. degree in engineering from Queen's University Belfast, U.K., in 2015.

He currently holds the Chair of Smart Energy Systems with the University of Leeds, Leeds, U.K. His research interests cover nonlinear system modelling, identification, and control, and machine learning, with substantial applications to energy and power systems, transport decarbonization, and energy management in energy intensive manufacturing processes.

Kaidi Li was born in Nanning, China, 1992. He received the B.E. degree in electrical engineering from Changsha University of Science and Technology, Changsha, China, in 2013, the M.S. degree in electrical engineering from the Central South University (CSU), Changsha, China, in 2016, and the Ph.D. degree in traffic equipment and information engineering from CSU, in 2019.

He is currently working with Shenzhen Metro Group Co., Ltd., Shenzhen, China. His research areas include fault diagnosis and fault tolerant control of power electronic converters.